

Retrieving the saddle-splay elastic constant K_{24} of nematic liquid crystals from an algebraic approach

Sébastien Fumeron

*Institut Jean Lamour, Université de Lorraine, BP 239,
Boulevard des Aiguillettes, 54506 Vandœuvre les Nancy, France and
Laboratoire d'Énergie et de Mécanique Théorique et Appliquée,
CNRS UMR 7563, Nancy Université, 54506 Vandoeuvre Cedex, France*

Fernando Moraes

*Departamento de Física, CCEN, Universidade Federal da Paraíba,
Caixa Postal 5008, 58051-900, João Pessoa, PB, Brazil and
Departamento de Física, Universidade Federal Rural de Pernambuco, 52171-900 Recife, PE, Brazil*

Erms Pereira*

*Escola Politécnica de Pernambuco, Universidade de Pernambuco,
Rua Benfica, 455, Madalena, 50720-001 Recife, PE, Brazil*

The physics of light interference experiments is well established for nematic liquid crystals. Using well-known techniques, it is possible to obtain important quantities, such as the differential scattering cross section and the saddle-splay elastic constant K_{24} . However, the usual methods to retrieve the latter involves an adjusting of computational parameters through the visual comparisons between the experimental light interference pattern or a ^2H-NMR spectral pattern produced by an escaped-radial disclination, and their computational simulation counterparts. To avoid such comparisons, we develop an algebraic method for obtaining of saddle-splay elastic constant K_{24} . Considering an escaped-radial disclination inside a capillary tube with radius R_0 of tens of micrometers, we use a metric approach to study the propagation of the light (in the scalar wave approximation), near to the surface of the tube and to determine the light interference pattern due to the defect. The latter is responsible for the existence of a well-defined interference peak associated to a unique angle ϕ_0 . Since this angle depends on factors such as refractive indexes, curvature elastic constants, anchoring regime, surface anchoring strength and radius R_0 , the measurement of ϕ_0 from the interference experiments involving two different radii allows us to algebraically retrieve K_{24} . Our method allowed us to give the first reported estimation of K_{24} for the lyotropic chromonic liquid crystal Sunset Yellow FCF: $K_{24} = 2.1 \text{ pN}$.

I. INTRODUCTION

Liquid crystals have invaded our everyday life, as witnessed by flat-display devices [1] or smart windows [2] based on polymer dispersed liquid crystals (PDLC) [3]. This is mainly due to their interesting dielectric and nematicoelastic properties, allowing the control of the director field configuration (Frederiks transitions) with a simple electric field [4]. The curvature elastic constants (K_{11} for splay, K_{22} for twist, K_{33} for bend and K_{24} for saddle-splay) for the spatial deformations of the nematic director field play a crucial role on the possible molecular configurations supported by each device [4]. If one is interested in the bulk region or near plane surfaces, only the constants K_{11} , K_{22} and K_{33} are relevant. However, when considering curved surfaces, as in droplets [5] or cylindrical cavities [6], the saddle-splay surface elastic constant K_{24} is important. The saddle-splay constant K_{24} is also a key parameter in the formation of topological defects [7–9] and when three-dimensional distortions appears in director patterns [10, 11].

The determination of K_{24} is usually based on two similar techniques relying on adjusting parameters involving computational simulations. Both of them use a capillary tube filled with a liquid crystal, which generates an escaped radial disclination in the nematic phase [12, 13]. Such configuration is strongly dependent on the saddle-splay constant K_{24} . The first technique uses micrometer-size cavities and it compares the interference pattern from experiments due to birefringence of the liquid crystal [14] with the one produced by computational simulations [15]. Tuning in the K_{24} in the computational simulations to match their interference pattern with the experimental ones, it is possible to

*Electronic address: erms.pereira@poli.br; On leave from: Instituto de Física, Universidade Federal de Alagoas, Av. Lourival Melo Mota, s/n, 57072-900, Maceió, AL, Brazil

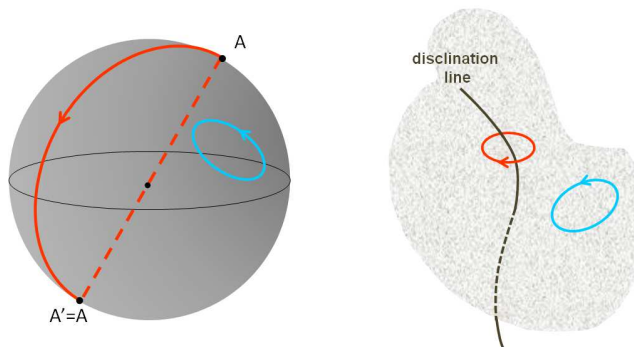


Figure 1: (*Left*) In the order parameter space, the two homotopy classes of $\pi_1(\mathbb{R}P^2)$. In blue, an ordinary closed loop homotopic to a point. In red, a closed contour terminating at two antipodal points A and A' : as both ends of the contour are fixed, it cannot be deformed to a point. (*Right*) In the real space (nematic), the two corresponding families of closed loops: red paths, which surround a disclination line, and blue paths which do not.

estimate K_{24} . The second technique uses submicrometer-size cavities and it compares the $^2H - NMR$ spectral pattern with its simulated counterpart [6]. Again, when the simulation matches the experimental pattern, it is assumed that K_{24} was set to the correct value.

In this paper, we theoretically propose an algebraic technique for the determination of K_{24} based on analogue gravity models, that has a good applicability on liquid crystals [16–24], used to describe the light propagation [17]. Its main asset is that it does not rely on comparisons between computational simulations and experiments at the micrometer scales. We determine theoretically the light interference pattern due to an escaped radial disclination [6, 13] by means of the partial wave method [17] for a confined liquid crystal sample in a capillary tube. Using the experimental value of the position ϕ_0 of the interference peak in our theoretical result, we can obtain the value of K_{24} and the surface anchoring strength S_0 . This is established in the one constant approximation ($K_{11} = K_{22} = K_{33} = K$) as well as out of it and we are not considering twist deformation for such disclination (for real systems, see [11, 25]).

This article is organized as follows. The next section reviews the stability of liquid crystalline defects and introduces the anchoring parameter σ , that links ϕ_0 to K_{24} in our study. In section III, we present the geometric approach for the light propagation in the nematic phase for different anchoring regimes. We also justify the choice of the liquid crystal at the cylindrical surface for the study of the interference pattern. Section IV presents the partial wave method developed from the geometrical approach, the definition of ϕ_0 in the experimental interference pattern and the procedure to retrieve K_{24} . We conclude by discussing some perspectives to this work.

II. STABILITY OF DEFECTS IN CONFINED MEDIA

Uniaxial nematic liquid crystals (UNLC) are mesophases formed by microscopic rod-like molecules. As a result of dipole-dipole interactions between them, these molecules orientate locally along a common direction given by a unit vector, the director \mathbf{n} . Moreover, they also exhibit a dimeric head-tail structure [26], such that macroscopic properties of UNLC remain statistically unchanged under $\mathbf{n} \leftrightarrow -\mathbf{n}$. Therefore, the region of variation of the director (called order parameter space \mathcal{M}) is the 2-sphere with antipodal points identified: in mathematics, this is known as the real projective plane $\mathbb{R}P^2$.

Following the pioneering works by Kleman, Toulouse, Michel and Volovik [27–29], a fruitful tool for studying defects in ordered media is provided by the homotopy theory. Generally speaking, homotopy groups of order parameter space $\pi_k(\mathcal{M})$ describe the topological properties of \mathcal{M} and their content determine the kind of defects supported by the medium. In the case of $\mathbb{R}P^2$, the non-trivial homotopy groups are

$$\pi_1(\mathcal{M}) = \mathbb{Z}/2\mathbb{Z} = \{0, 1\}, \quad \pi_2(\mathcal{M}) = \mathbb{Z}, \quad (1)$$

where $\pi_3(\mathcal{M}) = \mathbb{Z}$. Therefore, topologically stable point defects and linear defects (called disclinations) can appear. These latter arise because \mathcal{M} is not simply connected, e.g. there exist closed loops that cannot be contracted to a point. Indeed, $\pi_1 = \{0, 1\}$ contains two homotopy classes that correspond to the two kinds of closed loops existing on $\mathbb{R}P^2$ (Fig. 1). Homotopy class with topological charge 1 is associated with line defects of half-integer strength. On the contrary, elements of the trivial homotopy class with topological charge 0 are not stable defects: closed loops on $\mathbb{R}P^2$ can indeed smoothly be shrunk to a point, leading the director to have an uniform orientation.

Now, let us consider a capillary tube of radius R_0 filled with a nematic liquid crystal and assume homeotropic anchoring at the boundaries. The general form of the Frank-Oseen energy density writes:

$$F = \frac{1}{2} \iiint dV \left[K_{11} (\text{div } \mathbf{n})^2 + K_{22} (\mathbf{n} \cdot \text{curl } \mathbf{n})^2 + K_{33} (\mathbf{n} \times \text{curl } \mathbf{n})^2 + K_{13} \text{div } (\mathbf{n} \text{div } \mathbf{n}) - K_{24} \text{div } (\mathbf{n} \text{div } \mathbf{n} + \mathbf{n} \times \text{curl } \mathbf{n}) \right], \quad (2)$$

where K_{11} , K_{22} , K_{33} denote respectively the splay, twist and bend bulk elastic constants, K_{13} is the mixed splay-bend elastic modulus and K_{24} is the saddle-splay elastic constant. For simplicity, we consider weak deformations (the K_{13} term can be neglected) and isotropic elasticity ($K_{11} = K_{22} = K_{33} = K$). Thus, as anchoring is homeotropic, the simplest configuration minimizing F is a state of pure splay, i.e. $\mathbf{n} = \mathbf{e}_r$ [12], for which the surface saddle-splay term does not contribute. On the capillary axis, there is a linear singularity, the wedge disclination, of integer strength. From elasticity theory standpoint, the energetical cost per length of such defect is given by [30]

$$W = \pi K \ln \frac{R_0}{a}, \quad (3)$$

where a is a core cut-off parameter of order of molecular dimension: indeed, the elastic contribution of the core cannot be studied within the Frank-Oseen theory, as the director gradients are too large. In practice, this planar radial state costs too much energy (typically, $W \sim 10K$), so that such configuration is mechanically unstable. As such wedge disclination belongs to the trivial homotopy class, the director field gets out of the plane and tries to relax into the less expensive configuration of uniform orientation along the capillary axis (point in order parameter space): this is the well-known “escape into the third dimension” phenomenon. Ought to anchoring conditions at the boundaries, the orientation of \mathbf{n} cannot be exactly uniform and one is left with the three-dimensional escaped radial (ER) configuration (or splay-bend state) depicted in Fig. 2:

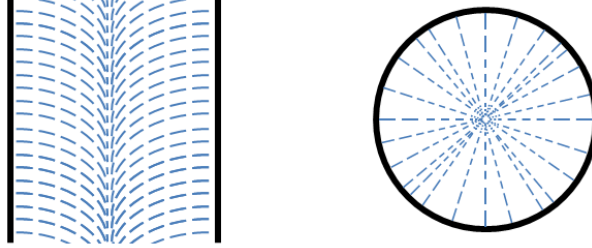


Figure 2: Front view and top view of the escaped radial configuration (homeotropic anchoring).

It must be noticed that ER can occur indifferently in the two opposite directions, as they are energetically equivalent. This can lead to the formation of additional point defects, which are metastable for long cylinders and energetically less favorable than pure ER configuration [31]: such configurations will thus be overlooked in the remainder of this article. Therefore, the energetic cost per length of such defect can be estimated as [6]

$$W = \pi K \left(3 - \frac{K_{24}}{K} - \frac{1}{\sigma} \right) \quad \sigma > 1, \quad (4)$$

$$= \pi K \left(\frac{R_0 S_0}{K} \right) \quad \sigma < 1. \quad (5)$$

Here, K_{24} is the surface elastic constant, S_0 is the surface density of interactions between the UNLC and the capillary tube, σ is the anchoring parameter defined as

$$\sigma = \frac{R_0 S_0}{K} + \frac{K_{24}}{K} - 1. \quad (6)$$

In case of strong anchoring, $S_0 \rightarrow \infty$, and so is σ . A modification of (6), out of the one constant approximation, can be found in the next section.

III. ANALOG MODEL FOR THE ESCAPED RADIAL DISCLINATION

A. General case

Classical geometrical optics can be summed up by the Fermat principle of least time, which states that light propagates along lines of shortest optical length. Usual nematic liquid crystals are generally uniaxial, which means that dielectric properties along the director's orientation (refractive index n_e) differ from those in a direction orthogonal to \mathbf{n} (refractive index n_o). This leads to the well-known phenomenon of birefringence, i.e. UNLC support two kinds of electromagnetic waves: ordinary rays (that experience only n_o) and extraordinary rays (that experience a refractive index combining n_o and n_e). Whereas ordinary light paths are trivial (as n_o is a constant), extraordinary light paths present more interesting properties. Indeed, electromagnetic energy conveyed by extraordinary light propagates according to a generalized form of Fermat principle [32]

$$\delta \left(\int N_r dl \right) = 0, \quad (7)$$

where dl is the euclidean element of arc length and N_r is the extraordinary ray index defined as

$$N_r^2 = n_o^2 \cos^2 \beta + n_e^2 \sin^2 \beta, \quad (8)$$

Here β denotes the local angle between the director \mathbf{n} and the unit vector \mathbf{T} tangent to the curves along which extraordinary energy is conveyed, and $\mathbf{n} \cdot \mathbf{T} = \cos \beta$ [16].

A very elegant and powerful approach to study light propagation in matter was first introduced by Gordon [33]. It was shown that a refractive medium acts on light in a similar fashion to a gravitational field: this is the core of the so-called analogue gravity models [34–36]. In this framework, optical paths correspond to the geodesics of an effective distorted geometry (technically a Riemannian manifold), so that one may identify the line element as [16]

$$ds^2 = N_r^2 dl^2 = g_{ij} dx^i dx^j, \quad (9)$$

where g_{ij} stands for the effective metric tensor. In this expression and in the remainder of this work, we follow Einstein's convention of summation over repeated indices. The curves along which light rays propagate are the solutions of the geodesic equations

$$\frac{d^2 x^i}{dt^2} + \Gamma_{jk}^i \frac{dx^j}{dt} \frac{dx^k}{dt} = 0, \quad (10)$$

where t is an affine parameter along the geodesic and the Γ_{jk}^i is the Christoffel connection symbol:

$$\Gamma_{jk}^i = \frac{g^{il}}{2} \left(\frac{\partial g_{lj}}{\partial x^k} + \frac{\partial g_{lk}}{\partial x^j} - \frac{\partial g_{jk}}{\partial x^l} \right). \quad (11)$$

Knowing the metric and Christoffel symbols allows us to determine not only the light paths, but also more global properties of the manifold. For example, the Ricci scalar R , which is a fair indicator of the curvature of the effective geometry. For more details on the geometric informations that can be extracted from a metric tensor, we refer the reader to classical textbooks on general relativity such as [37–39].

To determine the line element associated to extraordinary light, we will follow the elegant procedure proposed by Sátiro and Moraes [16]. We begin by expressing the position vector of light wave front

$$\mathbf{R} = \rho \cos \phi \mathbf{i} + \rho \sin \phi \mathbf{j} + z \mathbf{k}$$

and the unit tangent vector \mathbf{T} (parallel to the Poynting vector) is

$$\begin{aligned} \mathbf{T} &= \frac{d\mathbf{R}}{dl} = \cos \phi \frac{d\rho}{dl} \mathbf{i} + \sin \phi \frac{d\rho}{dl} \mathbf{j} + \frac{dz}{dl} \mathbf{k} - \\ &\quad - \rho \sin \phi \frac{d\phi}{dl} \mathbf{i} + \rho \cos \phi \frac{d\phi}{dl} \mathbf{j}, \\ &= \dot{\rho} \boldsymbol{\rho} + \rho \dot{\phi} \boldsymbol{\phi} + \dot{z} \mathbf{k}. \end{aligned}$$

The director orientation lies in the plane $\rho - z$, such that

$$\mathbf{n} = \sin \chi \boldsymbol{\rho} + \cos \chi \mathbf{k}, \quad (12)$$

where $\chi = \chi(\rho)$ is the angle between the director and the z-axis. Remembering that $\mathbf{n} \cdot \mathbf{T} = \cos \beta$ and that $\mathbf{n} \perp \phi$, the tangent vector \mathbf{T} simply writes, in the $\{\mathbf{n}, \phi\}$ basis, as

$$\mathbf{T} = \cos \beta \mathbf{n} + \sin \beta \phi. \quad (13)$$

This way, the inner product $\mathbf{n} \cdot \mathbf{T}$ generates

$$\cos \beta = \dot{\rho} \sin \chi + \dot{z} \cos \chi. \quad (14)$$

The norm of (13) gives $T^2 = 1 = \sin^2 \beta + \cos^2 \beta$, so that

$$\sin^2 \beta = \dot{\rho}^2 \cos^2 \chi + \rho^2 \dot{\phi}^2 - \dot{\rho} \dot{z} \sin 2\chi + \dot{z}^2 \sin^2 \chi. \quad (15)$$

Substituting (14)-(15) into (8) and then into (9), one obtains the following line element for the effective metric:

$$\begin{aligned} ds^2 &= N_r^2 dl^2, \\ &= (n_o^2 \sin^2 \chi + n_e^2 \cos^2 \chi) d\rho^2 + (n_e^2 - n_o^2) \sin 2\chi d\rho dz \\ &\quad + (n_o^2 \cos^2 \chi + n_e^2 \sin^2 \chi) dz^2 + n_e^2 \rho^2 d\phi^2. \end{aligned} \quad (16)$$

So this is the effective line element felt by the light near a escaped-radial disclination. As the angle χ depends on the kind of anchoring conditions (weak, strong) at the boundaries, these cases will be studied as follows.

B. Very weak anchoring

In the case of very weak anchoring $\sigma < 1$, then $\chi = 0$ everywhere. This is the case of full escape into third dimension and it leads to simplest form of the metric:

$$ds^2 = n_e^2 d\rho^2 + n_e^2 \rho^2 d\phi^2 + n_o^2 dz^2.$$

The Ricci scalar associated to this metric vanishes, which means that the geometry is flat: this was expected, as the rescaling $\tilde{\rho} = n_e \rho$ and $\tilde{z} = n_e z$ gives the euclidean line element. Therefore, light propagates along straight lines and no specific behavior of extraordinary light rays is expected for this configuration.

C. Weak and strong anchoring

In the case of weak anchoring $\sigma > 1$ and one-constant approximation, then following Crawford [6], the orientation of the director field is given by:

$$\chi(\rho) = 2 \tan^{-1} \left(\frac{\rho}{R_0} \tan \left(\frac{\alpha}{2} \right) \right). \quad (17)$$

with $\alpha = \arccos \frac{1}{\sigma}$ and

$$\lim_{\rho \rightarrow R_0} \chi(\rho) \equiv \chi_s = \cos^{-1} \frac{1}{\sigma}, \quad (18)$$

where σ is given by (6) and χ_s means the value of $\chi(\rho)$ at the surface of the tube. In the case of strong anchoring $\sigma \rightarrow \infty$, the previous expression for $\chi(\rho)$ results in

$$\chi(\rho) = 2 \tan^{-1} \frac{\rho}{R_0}, \quad (19)$$

where

$$\lim_{\rho \rightarrow R_0} \chi(\rho) = \frac{\pi}{2}.$$

The effective line element is obtained by substituting (17) (weak anchoring) or (19) (strong anchoring) in (16). However, $\chi(\rho)$ in the strong anchoring limit does not depend on the curvature elastic constants (at most, we can

obtain some knowledge about the refractive indices [17]). Thus the present study will be restricted to the case of weak anchoring.

We can obtain a generalization of (17) if $K_{11} \neq K_{33}$ (out of the one constant approximation). In such situation, $\chi(\rho)$ is the solution of

$$\begin{aligned} \frac{r}{R_0} &= \sqrt{\frac{\sigma+1}{\sigma-1} \frac{\Delta - \gamma' \cos \chi(\rho)}{\Delta + \gamma' \cos \chi(\rho)}} \\ &\times \exp\left(\frac{\gamma}{\gamma'} \sin^{-1}(\gamma \cos \alpha)\right) \\ &\times \exp\left(\frac{-\gamma}{\gamma'} \sin^{-1}(\gamma \cos \chi(\rho))\right), \quad \text{for } k > 1 \end{aligned} \quad (20)$$

or

$$\begin{aligned} \frac{r}{R_0} &= \sqrt{\frac{\sigma+1}{\sigma-1} \frac{\Delta - \gamma' \cos \chi(\rho)}{\Delta + \gamma' \cos \chi(\rho)}} \\ &\times \exp\left(\frac{\gamma}{\gamma'} \sinh^{-1}(\gamma \cos \alpha)\right) \\ &\times \exp\left(\frac{-\gamma}{\gamma'} \sinh^{-1}(\gamma \cos \chi(\rho))\right), \quad \text{for } k < 1 \end{aligned} \quad (21)$$

with

$$\lim_{\rho \rightarrow R_0} \chi(\rho) \equiv \chi_s = \cos^{-1}\left(\sqrt{\frac{k}{\sigma^2 + k - 1}}\right), \quad (22)$$

where $k = \frac{K_{33}}{K_{11}}$, $\Delta = \sqrt{1 - \gamma^2 \cos^2 \chi(\rho)}$, $\gamma^2 = |k - 1|/k$, $\gamma'^2 = 1/k$ and

$$\sigma = \frac{R_0 S_0}{K_{11}} + \frac{K_{24}}{K_{11}} - 1. \quad (23)$$

The algebraic plot of (17) (in the one constant approximation) and the numeric plots of (20) and (21) (out of the one constant approximation) are shown in Fig. 3. Observe that there is a good agreement among them near the surface of the capillary tube. Thus, for the sake of simplicity, we will consider that the solutions of Eqs. (20) and (21) can be approximately expressed by (17) with (22) and (23).

The previous consideration is enough to enable an algebraic study of the behavior of light, despite the rough calculations that can emerge from it. To get tractable results, we focus on the regions of the capillary tube that scatter light with the maximum of intensity. For this purpose, we define these regions as those where the effective space is the most curved, as prescribed by the values taken by the Ricci scalar R [37–39]. To localize those regions, we plot in Fig. 4 the Ricci scalar inside the capillary tube by substituting Eq. (17) into (16).

One observes that the Ricci scalar diverges near to the axis and close to the surface of the tube. The latter region is particularly relevant because, once

$$\lim_{\rho \rightarrow R_0} \chi(\rho) \equiv \chi_s,$$

we can extract some information about K_{24} through σ , using (18) for the one constant approximation or using (22) for a general case. In other words, we are interested in studying the light interfered by the liquid crystal at the cylinder surface with the angle between the director and the axis being $\chi(\rho = R_0) = \chi_s$.

Besides, ought to the cylindrical symmetry of the escaped-radial disclination, we restrict the study to planes $z = \text{const}$. Therefore, the line element (16) degenerates into

$$\begin{aligned} ds^2 &= (n_o^2 \sin^2 \chi_s + n_e^2 \cos^2 \chi_s) d\rho^2 + n_e^2 \rho^2 d\phi^2, \\ &= B^2 d\rho^2 + n_e^2 \rho^2 d\phi^2, \end{aligned}$$

where B is a constant given by $B^2 \equiv (n_o^2 \sin^2 \chi_s + n_e^2 \cos^2 \chi_s)$. Implementing the coordinate transformation $\tilde{\rho} = B\rho$ (which is equivalent to multiplying the line element by the conformal factor B^{-2}), the light trajectories and angles are preserved [38, 39], resulting in the following line element

$$ds^2 = d\tilde{\rho}^2 + b^2 \tilde{\rho}^2 d\phi^2, \quad (24)$$

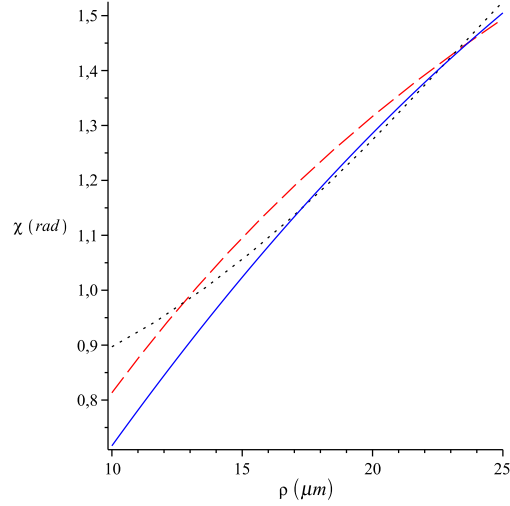


Figure 3: Angle χ between the director of liquid crystal E7 and the axis of the capillary tube with radius $R_0 = 25 \mu m$ for one constant approximation – blue solid line, Eq. (17) –, for $K_{11} \neq K_{33}$ with $k = \frac{K_{33}}{K_{11}} > 1$ – red dashed line, Eq. (20) – and for $K_{11} \neq K_{33}$ with $k = \frac{K_{33}}{K_{11}} < 1$ – black dotted line, Eq. (21).

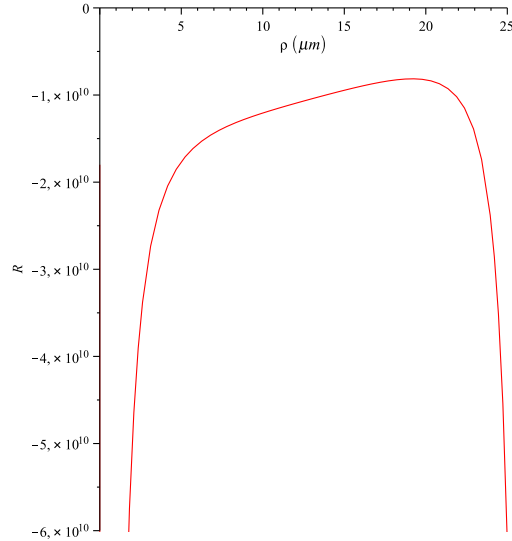


Figure 4: Ricci scalar of an escaped-radial disclination in a capillary tube with radius $R_0 = 25 \mu m$ filled with liquid crystal E7 anchoring weakly through Eq. (17).

with

$$b^2 = \frac{n_e^2}{(n_o^2 \sin^2 \chi_s + n_e^2 \cos^2 \chi_s)}. \quad (25)$$

Eq. (24) is the metric that will be used from now on to establish the light interference pattern due to the defect. It must be remarked that it is identical to the spatial segment of a global monopole's spacetime line element [40] in the equatorial plane $\theta = \frac{\pi}{2}$ (written in spherical coordinates).

IV. INTERFERENCE OF LIGHT

Usually, the study of an escaped radial disclination deals with numerical simulations combined with experimental data [6, 15, 41, 42]. In this section, we develop an analytic method to retrieve K_{24} from the partial wave method [43]

and afterwards, a comparison is made with the reported experimental data.

In the presence of a distorted spacetime, wave propagation is governed by the generalized form of D'Alembert scalar wave equation [38]

$$\nabla^\mu \nabla_\nu \Phi = \frac{1}{\sqrt{-g}} \nabla^\mu (\sqrt{-g} g^{\mu\nu} \nabla_\nu \Phi) = 0, \quad (26)$$

where Φ is the wave function, $g^{\mu\nu}$ are the components of the contravariant metric \mathbf{g} , $g = \det(\mathbf{g}_{\mu\nu})$. As usual, the Greek indices μ and ν are only used for the spacetime coordinates. To investigate the effect of the ER configuration on light waves, we replace the line element (24) into (26). Before starting the calculations, it must be emphasized that the analogue model developed in the previous section results in a spatial line element. However, a spacetime line element is needed in the D'Alembert equation. This problem is easily solved by using the fact that the geodesic equation and Fermat's principle produce the same results if they are used either with a spatial line element $d\tilde{s}^2$, such as (24), or a spacetime line element $ds^2 = -dt^2 + d\tilde{s}^2$ [38] ($c \equiv 1$), where $d\tilde{s}^2$ depends only on the spatial coordinates. Thus, line element (24) can be used without restrictions. Here we connect the ray optics to the wave optics by the eikonal approach [19, 32].

As usually done in interference problem with cylindrical symmetry, we seek solutions under the form of an expansion on partial waves

$$\Phi(t, \tilde{\rho}, \phi) = e^{-i\omega t} \sum_{l=0}^{\infty} a_l R_l(\tilde{\rho}) e^{il\phi}, \quad (27)$$

where ω is the angular frequency and a_l are constants. Substituting (27) into D'Alembert wave equation (26), we have

$$\frac{d^2 R_l}{d\tilde{\rho}^2} + \frac{1}{\tilde{\rho}} \frac{dR_l}{d\tilde{\rho}} + R_l \left(\omega^2 - \frac{\nu_l}{\tilde{\rho}^2} \right) = 0,$$

where $R_l(\tilde{\rho}) = J_{\nu_l}(\omega\tilde{\rho})$ is the Bessel function of the first kind (non-integer order) and $\nu_l = \frac{l}{b}$.

Following [17] and for a wave propagating in the x direction, the behavior of the wave function representing the scattered state, $v_\omega^{scatt}(\vec{r})$, will be

$$v_\omega^{scatt}(\vec{r}) \approx e^{i\omega x} + f(\phi) \frac{e^{i\omega\rho}}{\sqrt{\rho}},$$

where $e^{i\omega x} = e^{i\omega\rho \cos\phi} = \sum_{l=0}^{\infty} i^l \varepsilon_l J_l(\omega\rho) e^{il\phi}$ ($\varepsilon_0 \equiv 1$ and $\varepsilon_l \equiv 1 + e^{-2il\phi}$ for $l \geq 1$) according to the Jacobi-Auger expansion [44], $f(\phi)$ is the so-called *scattering amplitude* [43] and the factor $\sqrt{\rho}$ appears at the denominator to guarantee the conservation of the total energy flow. Thus, we should use the the following expression of the scattering amplitude $f(\phi)$ [17]:

$$f(\phi) = \frac{1}{\sqrt{\omega}} \sum_{l=0}^{\infty} i^l \varepsilon_l e^{il\phi} \sin(\delta_l) e^{i\delta_l}, \quad (28)$$

where the phase shift δ_l is

$$\delta_l(b) = \frac{l\pi}{2} \left(1 - \frac{1}{b} \right), \quad (29)$$

that is zero when $b = 1$. With values of b given by Eq. (25), we can implement a numerical plotting of the differential scattering cross-section $\sigma_{diff}(\phi)$ given by [43]

$$\sigma_{diff}(\phi) = \frac{d\sigma}{\sin\theta d\theta d\phi} = |f(\phi)|^2, \quad (30)$$

where an example is shown in Fig.5.

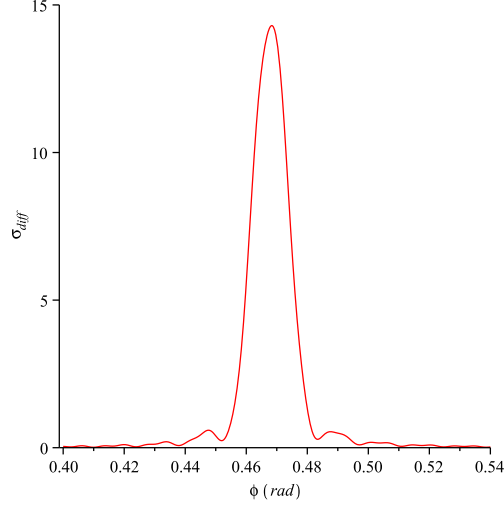


Figure 5: Differential scattering cross-section $\sigma_{diff}(\phi)$ for $b = 1.1759$ and eq. (28) truncated at $l = 450$. The angle of maximum interference ϕ_0 is close to 0.47 rad ($\approx 27^\circ$).

A. Algebraic approach

We can infer an algebraic expression for the angle of maximum interference in Fig. 5 by analyzing, following the steps shown in [17, 19], the light interference pattern created by the hedgehog topological defect with director $\hat{n} = \hat{r}$, in spherical coordinates, with effective spatial line element $ds^2 = dr^2 + \bar{b}^2 r^2 (d\theta^2 + \sin^2 \theta d\phi^2)$. Note the resemblance between this line element and the one in (24). In such situation, the scattering amplitude with spherical symmetry $f_s(\theta)$ (for a scalar wave propagating in the z direction) is [43]

$$f_s(\theta) = \frac{1}{2i\omega} \sum_{l=0}^{\infty} (2l+1) \left(e^{2i\delta_l^h} - 1 \right) P_l(\cos \theta) \quad (31)$$

and the phase shift for the hedgehog defect, δ_l^h , is [17, 19]

$$\delta_l^h(\bar{b}) = \frac{\pi}{2} \left(l + \frac{1}{2} - \frac{1}{\bar{b}} \sqrt{\left(l + \frac{1}{2} \right)^2 - \frac{1 - \bar{b}^2}{4}} \right). \quad (32)$$

For the case $\bar{b} \approx 1$, we can expand (32) in terms of $a^2 \equiv \frac{1 - \bar{b}^2}{4}$, resulting in

$$\delta_l^h(\bar{b}) \approx \frac{\pi}{2} \left(\alpha\gamma + \frac{a^2}{2\bar{b}\gamma} + O(a^4) \right), \quad (33)$$

where $\alpha \equiv 1 - \frac{1}{\bar{b}}$ and $\gamma \equiv l + \frac{1}{2}$. Substituting (33) in (31) we obtain $f_s(\theta) = f_s^{(0)}(\theta) + f_s^{(1)}(\theta) + \dots$, where [17, 19]

$$f_s^{(0)}(\theta) = \frac{1}{2^{3/2}\omega} \frac{\sin \pi\alpha}{[2(\cos \pi\alpha - \cos \theta)]^{3/2}}$$

and

$$f_s^{(1)}(\theta) = \frac{\pi\alpha^2}{2\bar{b}\omega} \frac{1}{\sqrt{2(\cos \pi\alpha - \cos \theta)}}.$$

From the last two equations, we notice that they diverge at the angle

$$\theta_0 = \pi\alpha = \pi \left(1 - \frac{1}{\bar{b}} \right), \quad (34)$$

observing that they don't depend on the wavelength λ of the light source. Thus, θ_0 is the angle of maximum intensity of the interfered light by the hedgehog defect.

Returning to the case of the escaped radial disclination, we notice that the angle of maximum interference, ϕ_0 , in Fig. 5 obeys the expression (34). Thus we will consider that the angle ϕ_0 of the maximum interfered light due to the liquid crystal at the surface of the capillary tube is also expressed by

$$\phi_0 = \pi \left(1 - \frac{1}{b} \right). \quad (35)$$

It is interesting to notice that our analytical procedure gives only the main peak position ϕ_0 , even though the numerical computation of Eq. (28) may be extended beyond $l = 450$ in order to get a better view of the secondary (and further) peaks shown in Fig. 5, that is a consequence of regarding light as a scalar wave.

From now on, we restrict our analysis to the case of $K_{11} \neq K_{33}$, ruled by (22) and (23). In order to obtain the angle ϕ_0 we need to feed the last equation with information found in the previous literature [15]. So, for the liquid crystal E7 confined in a capillary tube of radius $R_0 = 14.25 \mu m$, we find $b = 1.1759$ and $\phi_0 = 0.4699 \text{ rad}$ ($\approx 26.93^\circ$), which justifies the choice made in Fig. 5.

Once ϕ_0 depends on the radius of the capillary tube, due to its dependence on $\sigma(R_0)$, we can plot $\phi_0(R_0)$ to analyze its behavior. A log-linear graph of it is shown in Fig. 6.

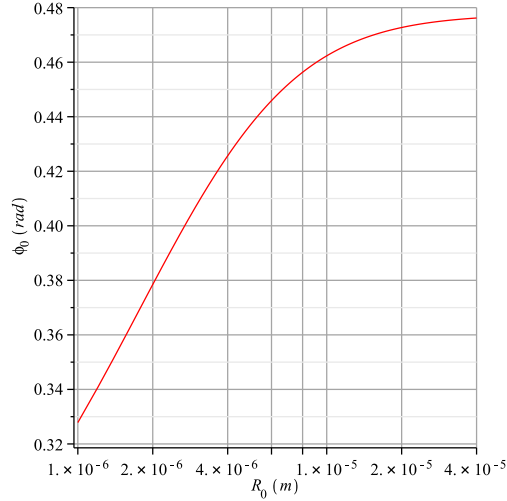


Figure 6: Log-linear behavior of the angle ϕ_0 of maximum interference on the radius of the capillary tube R_0 .

From Fig. 6, we observe a strong sensibility of ϕ_0 in the range $R_0 \in [1, 6] \mu m$. Beyond that, specially in the range $R_0 \in [10, 40] \mu m$, we notice a weak modification on $\phi_0 \in [0.46; 0.48] \text{ rad}$. It is on the latter range that we can compare our algebraic results with experimental data.

B. Comparison with experimental data

In the published literature, we find the details on the obtaining the experimental data of optical birefringence pattern created by general nematic director fields in cylindrical capillaries [30, 45–50] via optical polarizing microscopy and specifically by an escaped radial disclination [6, 15, 41, 51]. These birefringence patterns are produced for different orientations between the cylindrical axis and the polarization (analyzer) direction, represented by the angle α_0 in Fig. 7.

Once our geometric approach for light propagation deals with scalar waves and it produces only one maximum of interference, we compare our analytic result with the experimental and numerically simulated data for liquid crystal E7 confined in capillary tubes of radius $R_0 = 14.25 \mu m$ and $R_0 = 25.00 \mu m$ [15]. The details of the experimental setup and of the numerical calculations can be found in [51]. For $R_0 = 14.25 \mu m$, we feed Eqs. (23), (25) and (35) with information found in [15], resulting in $\sigma = 9.580$, $b = 1.1759$ and our algebraic prevision of maximum interference at the angle $\phi_0 \approx 26.93^\circ$. Considering that the spatial scales of the experimental textures and numerically simulated ones shown in Figs. 8 and 9 refer to a screen positioned at the wall of the capillary tube of radius R_0 , following the

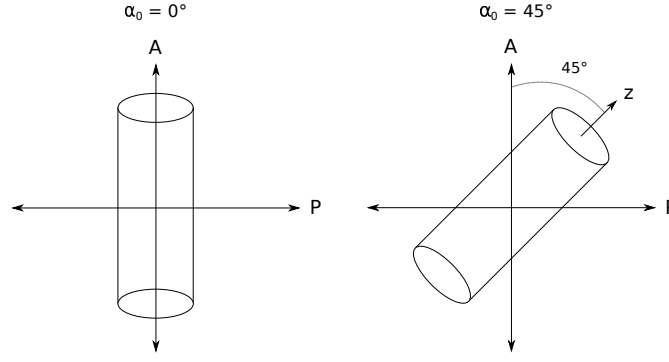


Figure 7: Orientations between the cylindrical axis and the analyzer for different angular apertures α_0 : (left) $\alpha_0 = 0^\circ$ and (right) $\alpha_0 = 45^\circ$.

experimental arrangement shown in [51], we can infer the angle of each maximum in those interference patterns and localize, by red lines in those figures, our forecast angle of maximum of interference at $\phi_0 = \pi \left(1 - \frac{1}{b}\right) \approx 26.93^\circ$ (the angular aperture from the center of the optical texture until the location of the forecast maximum of the differential scattering cross section). We observe that the calculated $\sigma = 9.58$, where it were used the experimental data from [15], is different from the simulated one, $\sigma_{sim} = 11$, needed to match the simulated texture with the experimental one. Once such discrepancy doesn't occur for the capillary tube with $R_0 = 25 \mu m$, as can be seen in the remaining of this section ($\sigma = 15.2$ and $\sigma_{sim} = 15$), we believe there was some mistype in [15] on the value of σ_{sim} for $R_0 = 14.25 \mu m$, that should be $\sigma_{sim} \approx 9.58$.

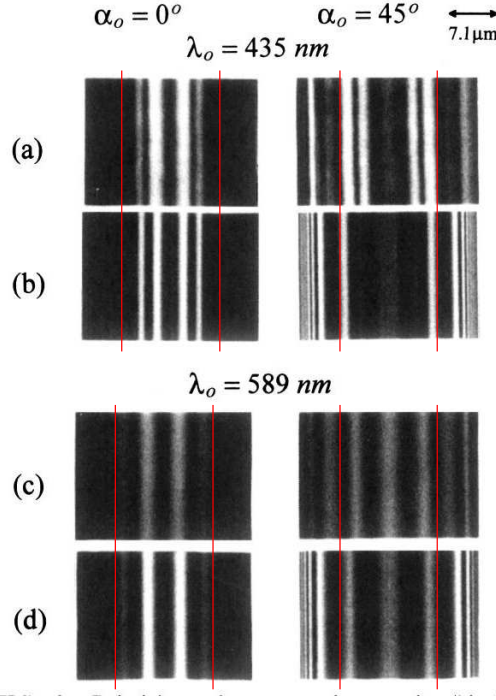


Figure 8: Extracted from [15]. Polarizing microscopy photographs (black and white) (a) and (c) compared with computer simulated results (b) and (d), all from [15], for a $R_0 = 14.25 \mu m$ capillary tube filled with the nematic liquid crystal E7 viewed between crossed polarizers (α_0 is the angle between the cylinder axis and the analyzer) using a monochromatic mercury light source, with wavelength $\lambda_0 = 435 nm$, (a) and (b) and sodium light source, with wavelength $\lambda_0 = 589 nm$, (c) and (d). The simulations correspond to $\sigma_{sim} = 11$. The red lines are the approximated indication of $\phi_0 = \pi \left(1 - \frac{1}{b}\right) \approx 26.93^\circ$, being the unique modification of the original picture extracted from [15].

For wavelength $\lambda_0 = 435 nm$ and $\alpha_0 = 45^\circ$, one observes that our algebraically predicted angle ϕ_0 is near to the outer end of the largest maximum of the experimental data (disregarding the central one) in Fig. 8a and it is near to

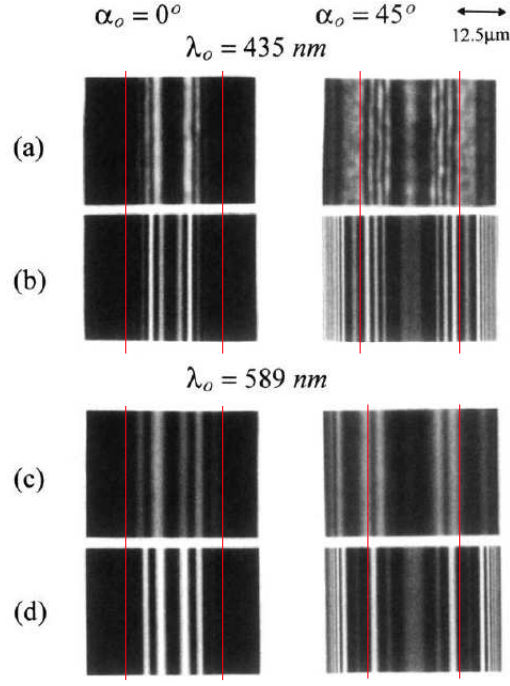


Figure 9: Extracted from [15]. Polarizing microscopy photographs (black and white) (a) and (c) compared with computer simulated results (b) and (d), all from [15], for a $R_0 = 25 \mu\text{m}$ capillary tube filled with the nematic liquid crystal E7 viewed between crossed polarizers (α_0 is the angle between the cylinder axis and the analyzer) using a monochromatic mercury light source, with wavelength $\lambda_0 = 435 \text{ nm}$, (a) and (b) and sodium light source, with wavelength $\lambda_0 = 589 \text{ nm}$, (c) and (d). The simulations correspond to $\sigma_{sim} = 15$. The red lines are the approximated indication of $\phi_0 = \pi(1 - \frac{1}{b}) \approx 27.19^\circ$, being the unique modification of the original picture extracted from [15].

the outer end of the correspondent computational predicted maximum in Fig. 8b. For wavelength $\lambda_0 = 589 \text{ nm}$ and $\alpha_0 = 45^\circ$, the algebraically predicted angle ϕ_0 is about at the middle point between two maxima of interference from the experimental data, as it can be seen in Fig. 8c, and it is near to outer end of the largest computational predicted maximum, as it can be seen in Fig. 8d. For $\alpha_0 = 0^\circ$, independent of the used wavelengths, the algebraically predicted angle ϕ_0 is far from any maximum of interference.

Before proceeding, a comment must be done about such results on the case of $\alpha_0 = 0^\circ$. The lack of matching between our analytic prevision and the computational or experimental data can be explained as an effect of the polarizing of light by the liquid crystal at the surface of the tube. Using the data of the liquid crystal E7 weakly anchoring in a capillary tube of $R_0 = 14.25 \mu\text{m}$, we obtain $\chi_s \approx 83^\circ$, that is almost perpendicular to the analyzer filter, justifying the absence of light at our predicted angle using $\alpha_0 = 0^\circ$. The same argument is valid for the next case, that uses a capillary tube of $R_0 = 25 \mu\text{m}$. Beyond that, the difference between the experimental and simulated patterns for $\alpha_0 = 45^\circ$ can be explained by the assumption made by the authors of [15, 51] in not considering the bend of light by the liquid crystal on the formation the interference pattern, as done in [17].

We implement another comparison using a capillary tube with $R_0 = 25 \mu\text{m}$ with E7, as it can be seen in Fig. 9. Again, for $\alpha_0 = 0^\circ$, there's no matching between $\phi_0 = \pi(1 - \frac{1}{b}) \approx 27.19^\circ$ ($\sigma = 15.2$, $b = 1.178$), and any of the maxima of light from experiment and simulation, independently of the used λ_0 . For $\alpha_0 = 45^\circ$ and $\lambda_0 = 435 \text{ nm}$, we see that the algebraically predicted angle ϕ_0 is near to the inner final of the largest maximum of interference in Fig. 9a and is near to the outer final of the largest computational predicted maximum in Fig. 9b. For $\lambda_0 = 589 \text{ nm}$, the algebraically predicted angle ϕ_0 it is near to the largest maximum of interference in Figs. 9c and 9d. The difference between Figs. 8 and 9 is a manifestation of the sensibility of the interference pattern on the radius R_0 of the capillary tube.

Finally the previous analysis allow one to define the approximate location of ϕ_0 in the experimental pattern: *near to the outer end of the largest maximum of interference pattern, using $\alpha_0 = 45^\circ$* . With that definition, we conclude that our single maximum of interfered light with angular position ϕ_0 always occurs in the experimental results and computational simulations shown in Figs. 8 and 9, extracted from [15]. From ϕ_0 , one obtains the saddle-splay elastic constant K_{24} , as shown in the next subsection. Observe that this definition was deliberately chosen so that our algebraically calculated K_{24} matches the value of the computationally obtained K_{24} of [15], where the latter results

are in agreement with their experimental measurements.

C. Determining the saddle-splay elastic constant K_{24}

Starting with the one constant approximation, we can use the presented algebraic method for ϕ_0 to determine S_0 and K_{24} . For that, we need to substitute the equations (25), (18) and (6) in (35) using the data of the studied liquid crystal, resulting in

$$\begin{aligned}\phi_0 &= \pi \left(1 - \frac{1}{b} \right) \\ &= \pi \left(1 - \frac{\sqrt{n_o^2 \left(1 - \frac{1}{\left(\frac{R_0 S_0}{K} + \frac{K_{24}}{K} - 1 \right)^2} \right) + \frac{n_e^2}{\left(\frac{R_0 S_0}{K} + \frac{K_{24}}{K} - 1 \right)^2}}}{n_e} \right).\end{aligned}\quad (36)$$

Thus, the substitution of two different pairs of R_0 and ϕ_0 (two experimental results of ϕ_0 for two different values of R_0) in (36) allows us to have a solvable system of two equations and two unknowns: $\frac{S_0}{K}$ and $\frac{K_{24}}{K}$. And if we have the value of K , (for example, through the approximation $K \approx \frac{K_{11} + K_{33}}{2}$ [15]), S_0 and K_{24} become completely determined.

Out of the one constant approximation and to form our system of equations with unknowns S_0 and K_{24} , we need additionally to know the values of the elastic constants K_{11} and K_{33} and to use the expressions (22) and (23). By this procedure, we would have an equivalent expression for (36) and we expect a better precision on the value of K_{24} (and eventually on S_0).

However, as we chose to study radii of the capillary tube in the range of weak sensibility on ϕ_0 , as shown in Fig. 6, there is a strong sensibility on the values of K_{24} and S_0 due to the measured ϕ_0 from the experimental data. A first way to bypass this problem is to use radii of capillary tubes smaller than $10 \mu m$, which corresponds to the region of strong sensibility for $\phi_0(R_0)$. Another possibility consists of using more than two capillary tubes to attribute to K_{24} and S_0 averaged values.

As a test of our approach, we use it to give the first reported estimation of K_{24} for the lyotropic chromonic liquid crystal (LCLC) Sunset Yellow FCF (SSY) [52–55]. From the light scattering data of wavelength $\lambda = 650 \text{ nm}$ for 31.5% (wt/wt) SSY at 298.15 K forming a twisted and escaped radial disclination [54] (that has a director field close to the capillary walls similar to the one of the escaped radial disclination), for 0.99 M SSY's refractive indices at 303.15 K and wavelength $\lambda = 633 \text{ nm}$ [55], our method gives $K_{24} = 2.1 \text{ pN}$. Despite having used different temperatures, wavelengths and concentrations of SSY on this estimation, the calculated value of SSY's K_{24} still obeys Ericksen's inequality $K_{22} + K_{24} \leq 2K_{11}$ [56] when using the experimental values of K_{11} ($K_{11} = 4.3 \text{ pN}$) and K_{22} ($K_{22} = 0.70 \text{ pN}$) found in [53]. We also report the first estimation of the the surface anchoring strength S_0 between SSY and parylene-N, material that was used in [54] to produce the homeotropic anchoring of the TER disclination: $S_0 = 5.5 \cdot 10^{-10} \text{ J/m}^2$.

V. CONCLUSIONS AND PERSPECTIVES

In this paper, we presented an algebraic method to retrieve the saddle-splay elastic constant K_{24} . Considering a metric approach for the propagation of light in an escaped radial disclination in a capillary tube, we identified that the liquid crystal at the surface of this tube can strongly scatter light. Using the effective metric felt by the light at this region in the d'Alembert scalar wave equation, we used the partial wave method to calculate the scattering amplitude, the differential scattering cross section and the possible angular positions where the latter diverges. We identified an unique universal angular position ϕ_0 , that is defined as the angle near the outer end of the largest maximum that composes the interference pattern of the experiment with $\alpha_0 = 45^\circ$, i.e., when the capillary tube makes simultaneously 45° with the crossed polarizer and analyzer. We showed that our ϕ_0 is algebraically related to K_{24} and to S_0 through eq. (36) in the one constant approximation and that a similar expression can be obtained if one is out of this approximation. Thus the localization of our algebraic ϕ_0 in the experimental light interference pattern allows us to obtain K_{24} and S_0 . A first application of our method allowed one to estimate the value of K_{24} for the lyotropic chromonic liquid crystal (LCLC) Sunset Yellow FCF (SSY) and the anchoring strength S_0 at the SSY–parylene-N interface.

This algebraic technique is an alternative to other methods that rely on comparisons between computational simulations of light interference pattern or $^2H - NMR$ spectral pattern with their experimental counterparts [15]. Our method has two steps: to localize our defined ϕ_0 in the experimental pattern of two different values of R_0 and to apply them in (36) to solve a system of two equations.

We believe that this procedure on measuring K_{24} will help on the engineering of the nematic configuration influenced by curved anchoring surfaces [3] and on the determination on the curvature energy in blue phases [4].

As a perspective of future studies, we could extend the presented algebraic method for sound waves [19], lowering the cost of the determination of K_{24} and S_0 .

Acknowledgements: FM thanks CNPq and CAPES (Brazilian agencies) for financial support. EP thanks CNPq and FAPESP (Brazilian agencies) for financial support.

All authors contributed equally to the paper.

-
- [1] D.-K. Yang and S.-T. Wu, *Fundamentals of Liquid Crystal Devices*, John Wiley, New Jersey, 2006.
 - [2] R. Baetens, B. P. Jelle and A. Gustavsen, *Solar Energy Materials and Solar Cells*, 2010, **94**, 87.
 - [3] J. Doane, *Liquid Crystals: Their Applications and Uses*, World Scientific, New Jersey, 1990.
 - [4] P. Oswald and P. Pieranski, *Nematic and cholesteric liquid crystals: concepts and physical properties illustrated by experiments*, CRC press, 2005.
 - [5] D. S. Miller and N. L. Abbott, *Soft Matter*, 2013, **9**, 374.
 - [6] G. Crawford, D. W. Allender and J. Doane, *Physical Review A*, 1992, **45**, 8693.
 - [7] P. Boltzenhagen, O. Lavrentovich and M. Kleman, *J. Phys. II France*, 1991, **1**, 1233.
 - [8] P. Boltzenhagen, M. Kleman and O. D. Lavrentovich, *J. Phys. II France*, 1994, **4**, 1439.
 - [9] P. Boltzenhagen, O. Lavrentovich and M. Kleman, *Physical Review A*, 1992, **46**, R1743.
 - [10] A. Sparavigna, O. D. Lavrentovich and A. Strigazzi, *Phys. Rev. E*, 1994, **49**, 1344–1352.
 - [11] E. Pairam, J. Vallamkondu, V. Koning, B. C. van Zuiden, P. W. Ellis, M. A. Bates, V. Vitelli and A. Fernandez-Nieves, *PNAS*, 2013, **110**, 9295–9300.
 - [12] P. Cladis and M. Kleman, *J. Physique*, 1972, **33**, 591.
 - [13] M. Kleman and O. D. Lavrentovich, *Soft Matter Physics: an introduction*, Springer-Verlag, New York, 2003.
 - [14] P. A. Kossyrev and G. P. Crawford, *Molecular Crystals and Liquid Crystals*, 2000, **351**, 379–385.
 - [15] R. D. Polak, G. P. Crawford, B. C. Kostival, J. W. Doane and S. Zumer, *Phys. Rev. E*, 1994, **49**, R978.
 - [16] C. Sátiro and F. Moraes, *Eur. Phys. J. E*, 2006, **20**, 173:1–6.
 - [17] E. Pereira and F. Moraes, *Liq. Cryst.*, 2011, **38**, 295–302.
 - [18] E. R. Pereira and F. Moraes, *Cent. Eur. J. Phys.*, 2011, **9**, 1100–1105.
 - [19] E. Pereira, S. Fumeron and F. Moraes, *Physical Review E*, 2013, **87**, 022506.
 - [20] S. Fumeron, B. Berche, F. Santos, E. Pereira and F. Moraes, *Phys. Rev. A*, 2015, **92**, 063806.
 - [21] S. Fumeron, E. Pereira and F. Moraes, *Physica B*, 2015, **476**, 19–23.
 - [22] S. Fumeron, E. Pereira and F. Moraes, *Int. J. Therm. Sci.*, 2013, **67**, 64–71.
 - [23] S. Fumeron, E. Pereira and F. Moraes, *Phys. Rev. E*, 2014, **89**, 020501.
 - [24] D. Melo, I. Fernandes, F. Moraes, S. Fumeron and E. Pereira, *Physics Letters A*, 2016, **380**, 3121 – 3127.
 - [25] A. A. Joshi, J. K. Whitmer, O. Guzman, N. L. Abbott and J. J. de Pablo, *Soft Matter*, 2014, **10**, 882–893.
 - [26] R. R. A.J. Leadbetter and C. Colling, *J. Phys. C1*, 1975, **36**, 37–43.
 - [27] M. Kleman and L. Michel, *Phys. Rev. Lett.*, 1978, **40**, 1387–1390.
 - [28] M. Kleman and G. Toulouse, *J. Phys. Lettres*, 1976, **37**, 149–151.
 - [29] G. Volovik and V. Mineev, *Sov. Phys. JETP*, 1977, **45**, 1186–1196.
 - [30] P. G. de Gennes and J. Prost, *The Physics of Liquid Crystals*, Clarendon Press, Oxford, 2nd edn, 1992.
 - [31] S. Burylov, *Sov Phys JETP*, 1997, **85**, 873–886.
 - [32] M. Born and E. Wolf, *Principles of optics: electromagnetic theory of propagation, interference and diffraction of light*, Cambridge university press, 1999.
 - [33] W. Gordon, *Annalen der Physik*, 1923, **377**, 421–456.
 - [34] P. Alsing, *American Journal of Physics*, 1998, **66**, 779–790.
 - [35] M. Novello and J. M. Salim, *Phys. Rev. D*, 2001, **63**, 083511.
 - [36] U. Leonhardt and P. Piwnicki, *Phys. Rev. Lett.*, 2000, **84**, 822–825.
 - [37] S. M. Carroll, *Spacetime and geometry*, Addison Wesley, San Francisco, 2003.
 - [38] C. W. Misner, K. S. Thorne and J. A. Wheeler, *Gravitation*, W. H. Freeman and Company, San Francisco, 1973.
 - [39] R. D’Inverno, *Introducing Einstein’s Relativity*, Oxford University Press, Oxford, 1998.
 - [40] A. Vilenkin and E. Shellard, *Cosmic strings and other topological defects*, Cambridge University Press, Cambridge, 1994.
 - [41] G. P. Crawford, J. A. Mitcheltree, E. P. Boyko, W. Fritz, S. Zumer and J. W. Doane, *Appl. Phys. Lett.*, 1992, **60**, 3226–3228.
 - [42] D. W. Allender, G. Crawford and J. Doane, *Physical review letters*, 1991, **67**, 1442.
 - [43] C. Cohen-Tannoudji, B. Diu and F. Laloe, *Quantum Mechanics*, Wiley-Interscience, New York, 1982, vol. 2.

- [44] G. B. Arfken, H. J. Weber and F. E. Harris, *Mathematical methods for physicists: A comprehensive guide*, Academic press, 7th edn, 2013.
- [45] R. B. Meyer, *Philosophical Magazine*, 1973, **27**, 405.
- [46] C. Williams, P. Pieranski and P. E. Cladis, *Phys. Rev. Lett.*, 1972, **29**, 90.
- [47] C. E. Williams, P. E. Cladis and M. Kleman, *Molecular Crystals and Liquid Crystals*, 1973, **21**, 355.
- [48] A. Saupe, *Molecular Crystals and Liquid Crystals*, 1973, **21**, 211.
- [49] M. Kleman, *Points, Lines and Walls in Liquid Crystals, Magnetic Systems and Ordered Media*, Wiley, New York, 1988.
- [50] M. Kuzma and M. M. Labes, *Molecular Crystals and Liquid Crystals*, 1983, **100**, 103.
- [51] A. Scharkowski, G. P. Crawford, S. Zumer and J. W. Doane, *J. Appl. Phys.*, 1993, **73**, 7280.
- [52] S.-W. Tam-Chang and L. Huang, *Chemical Communications*, 2008, 1957–1967.
- [53] S. Zhou, Y. A. Nastishin, M. Omelchenko, L. Tortora, V. Nazarenko, O. Boiko, T. Ostapenko, T. Hu, C. Almasan, S. Sprunt *et al.*, *Physical review letters*, 2012, **109**, 037801.
- [54] J. Jeong, L. Kang, Z. S. Davidson, P. J. Collings, T. C. Lubensky and A. Yodh, *Proceedings of the National Academy of Sciences*, 2015, **112**, E1837–E1844.
- [55] V. R. Horowitz, L. A. Janowitz, A. L. Modic, P. A. Heiney and P. J. Collings, *Physical Review E*, 2005, **72**, 041710.
- [56] J. Ericksen, *Physics of Fluids (1958-1988)*, 1966, **9**, 1205–1207.